High-field magnetospectroscopy to probe the 1.4-eV Ni color center in diamond

P. Plochocka,[1,2,*] O. Portugall,[1] P. Y. Solane,[1] E. Gheeraert,[3] L. Ranno,[3] E. Bustarret,[3] N. Bruyant,[1] I. Breslavetz,[2] D. K. Maude,[2] H. Kanda,[4] and G. L. J. A. Rikken[1]

[1]*Laboratoire National des Champs Magnétiques Intenses, CNRS-UJF-UPS-INSA, 143, avenue de Rangueil, 31400 Toulouse, France*

[2]*Laboratoire National des Champs Magnétiques Intenses, CNRS-UJF-UPS-INSA, 25 rue des Martyrs 38042 Grenoble, France*

[3]*Institut Néel, CNRS and Université Joseph Fourier, 25 rue des Martyrs 38042 Grenoble, France*

[4]*National Institute for Materials Science, 1-1 Namiki, 305-0044 Tsukuba, Japan*

(Received 5 March 2012; revised manuscript received 14 May 2012; published 9 July 2012)

A magneto-optical study of the 1.4-eV Ni color center in boron-free synthetic diamond, grown at high pressure and high temperature, has been performed in magnetic fields up to 56 T. The data are interpreted using the effective spin Hamiltonian of Nazaré, Nevers, and Davies [Phys. Rev. B **43**, 14196 (1991)] for interstitial Ni^+ with the electronic configuration $3d^9$ and effective spin $S = 1/2$. Our results unequivocally demonstrate the trigonal symmetry of the defect, which preferentially aligns along the [111] growth direction on the (111) face, but reveal the shortcomings of the crystal field model for this particular defect.

DOI: 10.1103/PhysRevB.86.045203 PACS number(s): 71.55.−i, 78.55.−m

I. INTRODUCTION

Diamond, as a material, has attracted a lot of attention due to its unique physical properties; it is the hardest known material with high thermal conductivity and a 5.5-eV-wide electronic band gap. The large Debye temperature of diamond reduces the interaction between impurities and the lattice, leading to almost atomiclike optical emission spectra of defects with extremely narrow lines. The so-called color centers, various transition-metal-nitrogen/vacancy complexes in diamond, can act as single-photon sources, capable of photostable operation at room temperature,[1–4] with possible applications in quantum information processing.[5] Moreover, the nitrogen/vacancy (NV) center in diamond has been used to image a single electronic spin using nanoscale magnetometry.[6,7] The NV center has also been used to produce diamond-based light-emitting diodes.[8] These developments have led to a renewed interest in the optical properties of color centers in diamond.

Macroscopic synthetic diamond crystals are mainly grown by chemical-vapor deposition (CVD) methods or by the high-pressure high-temperature (HPHT) method, the latter giving mm^3-size bulk crystals. In both growth techniques, there are only a few impurities which can enter into the diamond structure. Using the HPHT method, the incorporation of cobalt[9] (Co) or nickel[10,11] (Ni) has been achieved in significant amounts. Incorporating transition metals into diamond is of interest for applications such as single-photon emitters[1–4] or spintronics in analogy to diluted magnetic semiconductors (DMS). The Curie temperature of DMS has been predicted to scale with the inverse cube of the lattice constant of the host matrix.[12] Diamond has the smallest lattice constant ($a = 3.56$ Å) of all semiconductors, making it an excellent candidate for ferromagnetic ordering above room temperature. For all these reasons, a thorough understanding of transition-metal complexes in diamond has become essential to further develop diamond-related technologies.

Despite the numerous potential applications of the nickel color center in diamond, its exact crystallographic site and electronic properties are still under debate. The NIRIM-2 electron spin resonance (ESR) line[13] has been identified with the 1.4-eV doublet of zero-phonon lines (ZPLs) seen in optical studies,[14–18] and unambiguously attributed to a nickel-containing center.[14,15] The ESR results suggested that the nickel is incorporated interstitially in a single positively charged state $3d^9$, effective spin $S = 1/2$ with trigonal symmetry and a strong trigonal distortion due to the presence of an additional impurity or vacancy nearby.[13] The trigonal symmetry was confirmed by optical studies[15] under uniaxial stress and magnetic fields up to 6 T. The agreement between the ESR and magneto-optical data has led some authors to propose that the Zeeman splitting of the 1.4-eV line be used as a pulsed magnetic field calibration probe.[18] However, recent studies suggested an alternative complex of nickel with boron,[19] or even isolated interstitial Ni.[20] Recent theoretical work also contradicts the hypothesis of either isolated interstitial Ni or interstitial Ni complex with either a vacancy or an impurity; the calculations predict that interstitial Ni with trigonal symmetry is unstable.[21]

In order to further elucidate the nature of this defect, we have performed a magneto-optical study of the Ni color center in synthetic diamond, which is characterized by two zero-phonon lines (ZPLs) at $\simeq$1.401 and $\simeq$1.404 eV. Measurements in high magnetic fields unequivocally demonstrate the trigonal symmetry of the defect which is mostly incorporated on the (111) faces with its trigonal axis preferentially aligned along the growth direction. For incorporation on the (001) face, there is no preferential alignment of the defect axis along one of the four ⟨111⟩ directions. These results are extremely well described by the effective spin Hamiltonian for a trigonal defect proposed in the seminal paper of Nazaré, Nevers, and Davies[15] (hereafter referred to as NND) using a single-parameter set for both the (111) and (001) faces. However, in certain regions of the (111) face, the trigonal axis of the defect is not preferentially aligned. Under such conditions, the correct parameters of the effective spin Hamiltonian are significantly different.

II. SAMPLE CHARACTERIZATION

Two diamond crystals containing nickel and nitrogen have been studied. The crystals were grown in nickel solvent in

similar high-pressure and high-temperature conditions, except that for one of the crystals a nitrogen getter (Ti) was added to the solvent in order to reduce the nitrogen incorporation. Crystal KA1970 (sample A), grown with the nitrogen getter, has a light green color and KA1153 (sample B), grown without the nitrogen getter, has a yellow/brown color. As there was no specific boron contamination of the growth environment, the concentration of this impurity is expected to be negligible in the grown crystals. Both single crystals have mainly wide (111) growth sectors, with smaller (001) growth sectors terminated by square faces. The type-Ib diamond seed crystals were not removed. According to the growth conditions, the nickel concentration is expected to be around 10^{19} cm^{-3} in both crystals, and the nitrogen concentration around 10^{17} cm^{-3} in sample A and 10^{19} cm^{-3} in sample B. Due to the dependence of the impurity incorporation rate on the crystallographic orientation during growth, the impurity concentration is expected to depend on the growth sector. Crystals were characterized by cathodoluminescence at $T = 5$ K with a 30-kV e-beam and magnetometry using a SQUID magnetometer in the temperature range 2 to 300 K and in a 0 to 5 T magnetic field.

A. Cathodoluminescence

For sample B, grown without the nitrogen getter, the cathodoluminescence spectra recorded on (100) and (111) growth sectors exhibits mainly the 1.40-eV center (Fig. 1), which can be attributed unambiguously to a defect containing a single nickel atom.[14] Nitrogen-related centers H3 (2.46 eV, attributed to nitrogen VNV complex) and 2.156 eV (attributed to neutral NV complex) also appeared, but with stronger H3 signal on the (100) sectors and stronger 2.156-eV signal on (111) sectors. A nickel-related peak at 2.56 eV was also observed on the (111) growth sector, suggesting a stronger incorporation of Ni in the (111) growth sectors, in agreement with previous studies. Note that no signal corresponding to W8 centers, related to substitutional Ni_s^-, were observed.[22,23] For sample A, grown with the nitrogen getter, the intensity of the 1.40-eV lines is significantly larger compared to sample B. Spectra recorded on the (111) growth sector reveal the 2.56-eV Ni-related center, with very weak N-related signals. This suggests a much stronger incorporation of Ni in (111) growth sectors compared to (100).

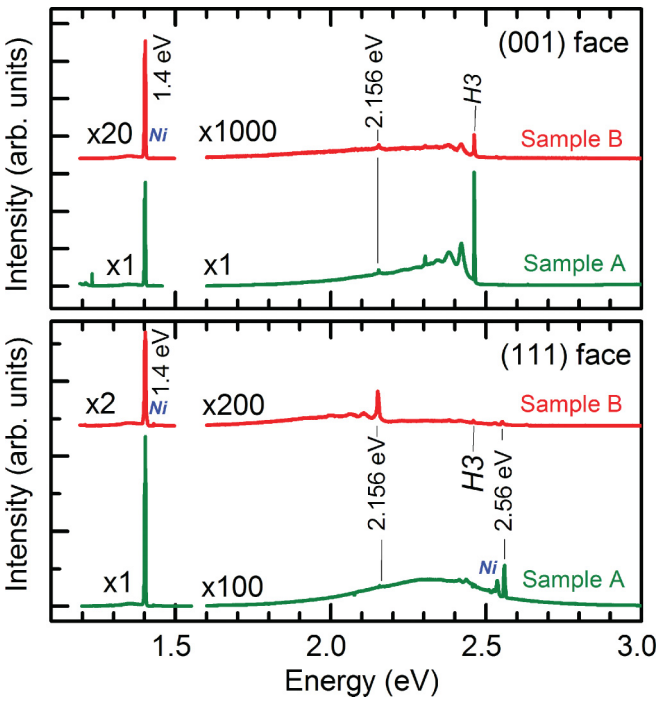

FIG. 1. (Color online) Cathodoluminescence spectra of sample A (grown with N getter) and sample B (grown without N getter) recorded on (100) and (111) growth sectors under similar conditions.

B. Magnetization

Information concerning the incorporation of Ni can also be obtained from magnetization measurements. Between room temperature and $\simeq$100 K, the magnetic moment of sample B is proportional to field [Fig. 2(a)] with a negative slope, i.e., negative susceptibility of $\chi = -2.5 \times 10^{-5}$. This is close to the diamagnetic susceptibility of diamond ($\chi = -2.2 \times 10^{-5}$) and as expected shows no temperature dependence. Below 100 K, an additional contribution appears, increasing in intensity as the temperature decreases. This contribution is attributed to a paramagnetic component. This assignment is confirmed by the good agreement [see Fig. 2(a)] with a

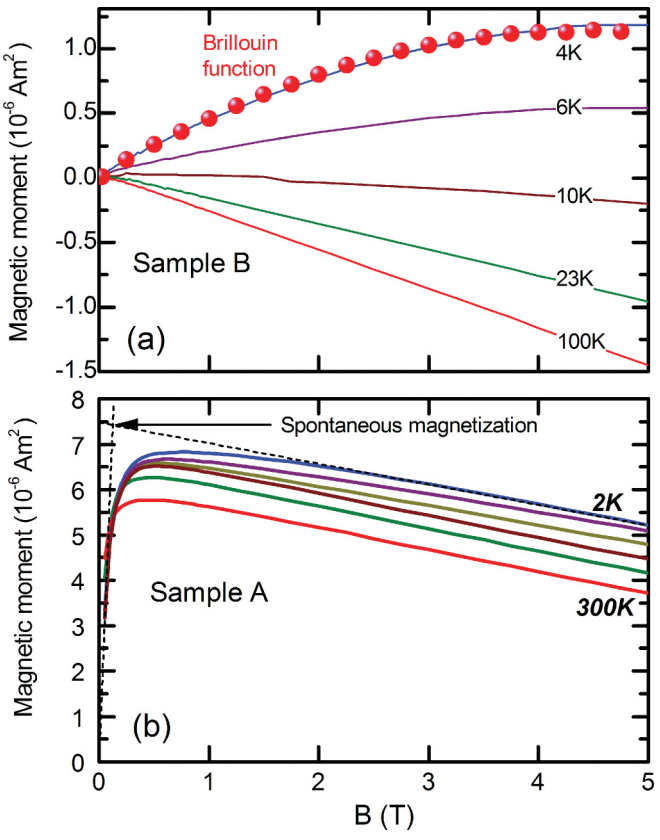

FIG. 2. (Color online) (a) SQUID measurement of sample B. The symbols show a fit using a Brillouin function as described in the text. (b) SQUID measurement of sample A at temperatures 300, 200, 50, 10, 4, and 2 K. The broken lines indicate the method used to determine the spontaneous magnetization $M(T)$.

Brillouin function approach

$$B_J(x) = \frac{2J+1}{2J}\coth\left(\frac{2J+1}{2J}x\right) - \frac{1}{2J}\coth\left(\frac{x}{2J}\right), \quad (1)$$

with

$$x = \frac{gJ\mu_B B}{kT} \quad (2)$$

and the total magnetic moment being

$$m(B) = N_{\mathrm{Ni}} g J \mu_B B_J(x), \quad (3)$$

where J is the Ni quantum number, g the Landé factor, μ_B the Bohr magneton, k the Boltzmann constant, T the temperature, N_{Ni} the concentration of paramagnetic centers, and B the applied magnetic field. The fit was performed assuming $gJ = 2$ and leaving N_{Ni} as the only free parameter. A value of $gJ = 2$ corresponds to isolated nickel in the Ni_2^+ oxidation state ($3d^8$), assuming $J \approx S \approx 1$ and $g = 2$. A concentration of paramagnetic centers $N_{\mathrm{Ni}} = 1.5 \times 10^{19}$ cm^{-3} was deduced. Note, a value of $gJ = 3$ ($J = 3/2$) or lower value $gJ = 1$ ($J = 1/2$) would reduce or increase N_{Ni} accordingly. Nevertheless, this concentration is in the order of magnitude of the expected incorporated Ni concentration. Such a value corresponds to a Ni relative concentration of 8×10^{-5}, i.e., a very diluted magnetic system in which weak interactions between magnetic ions and a paramagnetic behavior are expected. We deduce that nickel is incorporated as isolated, noninteracting paramagnetic centers.

For sample A, the magnetic moment has a very different behavior, as seen in Fig. 2(b). A magnetic field as low as 0.5 T is already sufficient to saturate the magnetic moment even at 300 K, suggesting a ferromagnetic behavior. The linear decrease observed for higher fields is attributed, as before, to the diamagnetic contribution of the diamond matrix. Plots representing the reduced magnetization $M(T)/M_S$ as a function of the reduced temperature T/T_c should be similar for bulk nickel and for this ferromagnetic sample. Under such an assumption, the temperature dependence of the experimental magnetization (Fig. 3) corresponds to a 500-K Curie temperature, 20% smaller than the one of bulk nickel (631 K). This suggests the presence of nickel clusters, with a reduced Curie temperature due to size effects. The low-temperature spontaneous magnetic moment of $M_S = 7.4 \times 10^{-6}$ Am^2 gives a nickel concentration of $N_{\mathrm{Ni}} = 3.5 \times 10^{19}$ cm^{-3}, assuming a $gJ = 2$, which has the same order of magnitude as for sample B.

The strikingly different magnetic behavior of both samples indicates the strong influence of nitrogen on the incorporation of Ni in diamond. Without nitrogen (i.e., with a much lower N concentration than Ni concentration), as in sample A, Ni tends to form clusters, reducing the concentration of isolated nickel and the crystal is ferromagnetic. With nitrogen, no ferromagnetic behavior is observed, and the nickel atoms are diluted into the crystal as paramagnetic centers. This suggests a lower formation energy for Ni-N complexes compared to Ni defects such as interstitial Ni, substitutional Ni, and NiV. This is in agreement with first-principles theoretical investigation of nickel-related complexes in diamond.[21]

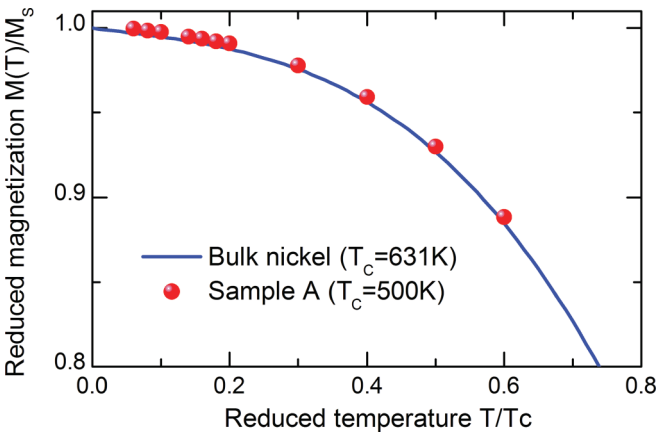

FIG. 3. (Color online) Reduced magnetic moment $M(T)/M_S$ versus reduced temperature for bulk nickel (line) and sample A (symbols), drawn for $T_c = 631$ K for nickel and $T_c = 500$ K for sample A.

III. EFFECTIVE SPIN HAMILTONIAN

Before presenting the magnetophotoluminescence results, we briefly outline the NND effective spin Hamiltonian[15] for trigonal interstitial Ni^+ with the electronic configuration $3d^9$ and effective spin $S = 1/2$, which is required to understand the data. We note that a similar Hamiltonian has been proposed to describe trigonal Cr in GaAs.[24,25] The principal crystallographic orientations of the HPHT diamond crystals investigated here are presented schematically in Fig. 4. It is possible to define four sets of local axes Z, X, Y (see Table I) corresponding to the four different possible ⟨111⟩ orientations of the trigonal axis of the defect. The quantization axis Z is parallel to the C_3 axis. The perturbation of the magnetic field is given by the following Hamiltonian:

$$\Delta H = \mu_B(g_1 B_X S_X + g_1 B_Y S_Y + g_3 B_Z S_Z), \quad (4)$$

where μ_B is the Bohr magneton and the quantization axis is the Z trigonal axis of the center.

The energy separation of the excited and ground states is large enough to ignore any interaction between them. The

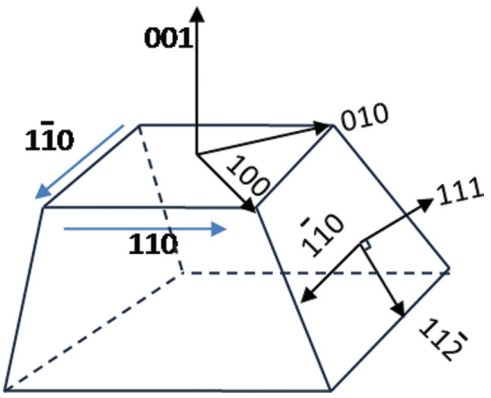

FIG. 4. (Color online) Simplified schematic of the HTHP synthetic diamond crystals labeling the principal crystallographic axes. The small (113) and (101) faces of our cubo-octahedral crystal have been omitted for clarity.

secular matrix describing the perturbation of the magnetic field on the ground-state doublet is

$$\frac{1}{2}\begin{pmatrix} g_3'\mu_B B_Z+\lambda & 0 & 0 & g_1\mu_B B_X - ig_1\mu_B B_Y \\ 0 & -g_3'\mu_B B_Z+\lambda & g_1\mu_B B_X - ig_1\mu_B B_Y & 0 \\ 0 & g_1\mu_B B_X + ig_1\mu_B B_Y & g_3\mu_B B_Z-\lambda & 0 \\ g_1\mu_B B_X + ig_1\mu_B B_Y & 0 & 0 & -g_3\mu_B B_Z-\lambda \end{pmatrix}, \tag{5}$$

where $\lambda \simeq 2.8$ meV is the spin-orbit splitting of the ground state and the various g terms are the effective Landé g factors. The secular matrix describing the excited state in a magnetic field is given by

$$\frac{1}{2}\mu_B \begin{pmatrix} g_3^e B_Z & g_1^e B_X - ig_1^e B_Y \\ g_1^e B_X + ig_1^e B_Y & -g_3^e B_Z \end{pmatrix}. \tag{6}$$

The secular matrices can easily be diagonalized either numerically or analytically. We have done both and verified that the results are identical. The analytic expressions for the ground and excited states are

$$\begin{aligned} E^g_{1,2} &= \tfrac{1}{2}\mu_B\Big[\mp\tfrac{1}{2}B_Z(g_3-g_3') \\ &\quad -\sqrt{g_1^2\left(B_X^2+B_Y^2\right)+\left(\lambda\pm\tfrac{1}{2}B_Z(g_3'+g_3)\right)^2}\Big], \\ E^g_{3,4} &= \tfrac{1}{2}\mu_B\Big[\mp\tfrac{1}{2}B_Z(g_3-g_3') \\ &\quad +\sqrt{g_1^2\left(B_X^2+B_Y^2\right)+\left(\lambda\pm\tfrac{1}{2}B_Z(g_3'+g_3)\right)^2}\Big], \\ E^e_{1,2} &= \pm\tfrac{1}{2}\mu_B\sqrt{\left(g_1^e\right)^2\left(B_X^2+B_Y^2\right)+B_Z^2\left(g_3^e\right)^2}. \end{aligned} \tag{7}$$

The magnetic field lifts the degeneracy of the ground and excited states, which split into four and two levels, respectively. The energy of the possible optical transitions is simply the energy difference between all levels in the ^2A excited state and all levels in the ^2E ground state. Thus, taking into account the four possible orientations of the defect axis (see Table I), we expect a maximum of 32 lines in the spectrum depending upon the orientation of the magnetic field. When the magnetic field is aligned along a symmetry axis, the number of transitions with different energies is greatly reduced.

IV. MAGNETOPHOTOLUMINESCENCE

Micro-photoluminescence (μ-PL) in dc magnetic fields up to 28 T and macro-photoluminescence (PL) in pulsed magnetic field up to 56 T have been performed. For both experiments, an optical fiber was used for the excitation and collection of the emission from the sample. A Continuous Wave (CW) Ti:sapphire laser tuned to 720 nm or a CW solid-state laser at 660 nm was used for the excitation. The emission spectra have been measured using a spectrometer equipped with a CCD camera. For the macro-PL, the sample was placed at the end of the fiber with a diameter of 50 μm^2. In μ-PL measurements, light was focused on the sample using a microscope objective coupled with a monomode fiber. The size of the laser spot on the sample was around 1 μm^2. The sample was mounted on piezo translation stages, which allow spectrally resolved spatial mapping in magnetic field. The measurements were performed at $T \simeq 4$ K with the magnetic field applied parallel to (Faraday configuration) and normal to (Voigt configuration) the direction of propagation of the light. A number of different orientations of the crystal with respect to magnetic field have been measured on the (111) and (001) faces. Typical optical spectra, for both samples, measured at low temperature and at zero magnetic field are presented in Fig. 5. A characteristic zero-phonon doublet is observed at ≃1.401 and ≃1.404 eV. The doublet structure originates from the $\lambda \simeq 2.8$ meV splitting of the (^2E) ground state due to a combination of spin-orbit interaction and trigonal distortion. The asymmetric line shape is the result of unresolved Ni isotopic splitting.[15] For sample A, representative spectra recorded at two different locations are shown. The small shift of the energetic position

TABLE I. Summary of the four possible orientations of the local (ZXY) axis of the trigonal defect along the ⟨111⟩ directions. The different orientations are labeled $\alpha,\beta,\gamma,\delta$.

Label	Z	X	Y
α	[111]	[11$\bar{2}$]	[1$\bar{1}$0]
β	[1$\bar{1}$1]	[1$\bar{1}\bar{2}$]	[$\bar{1}\bar{1}$0]
γ	[$\bar{1}\bar{1}$1]	[$\bar{1}\bar{1}\bar{2}$]	[$\bar{1}$10]
δ	[$\bar{1}$11]	[$\bar{1}$1$\bar{2}$]	[110]

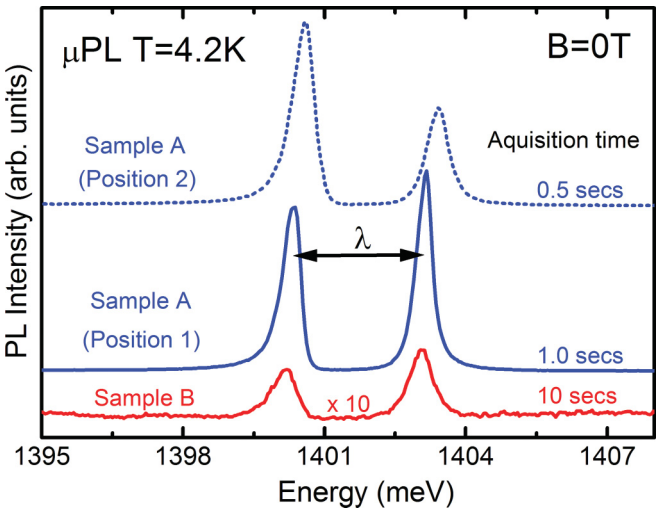

FIG. 5. (Color online) Typical μ-photoluminescence spectra (zero-phonon doublet) of Ni incorporated in HPHT synthetic diamond for samples A (at two different positions) and B at $T = 4.2$ K and $B = 0$ T. All spectra are taken on the (111) face. A linear background has been subtracted from the rather weak PL signal of sample B and the curves are offset vertically for clarity. Position 2 is close to the bottom of the (111) face, i.e., near the seed crystal. See μ-PL map in Fig. 11.

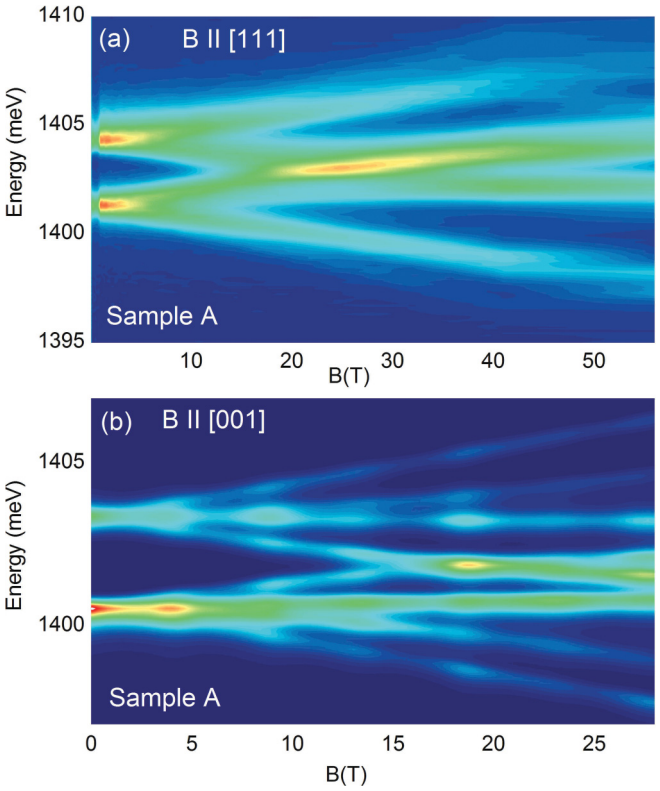

FIG. 6. (Color online) Representative $T = 4.2$ K magnetophotoluminescence spectra in the Faraday configuration of the 1.4-eV Ni color center in HPHT synthetic diamond. (a) Macro-PL with $B \parallel [111]$ collected from the (111) face. (b) μ-PL with $B \parallel [001]$ collected from the (001) face. Please note the different magnetic field ranges.

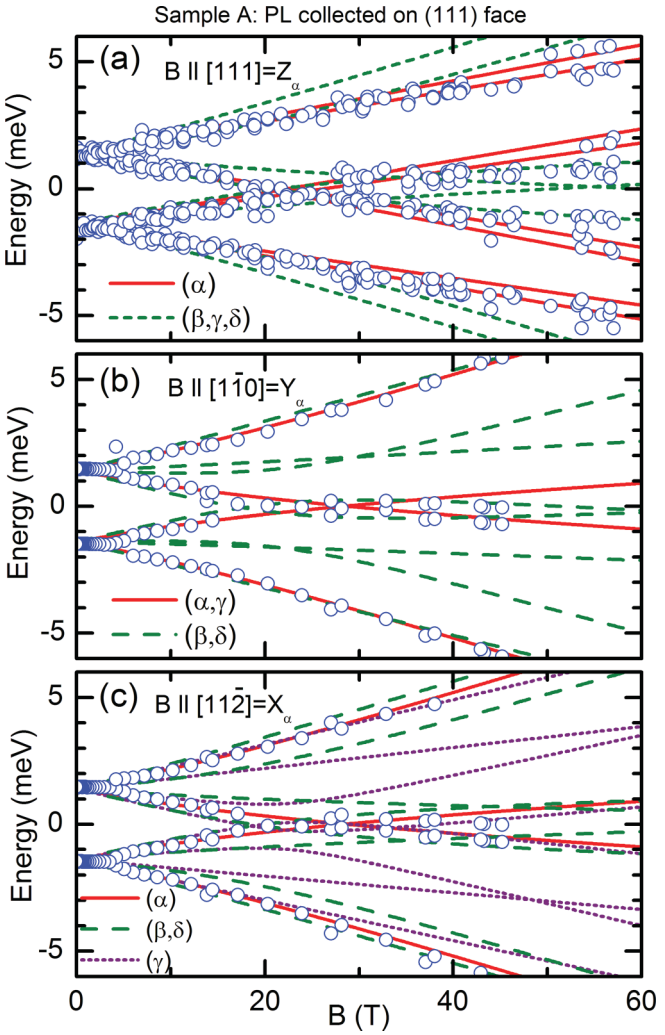

FIG. 7. (Color online) Energy of the transitions (symbols) for photoluminescence collected from the (111) face of the diamond crystal (sample A) as a function of the magnetic field applied parallel to the [111], [1$\bar{1}$0], and [11$\bar{2}$] directions. The transition energies calculated with the effective spin Hamiltonian are shown as red solid lines for a defect axis aligned along the [111] growth direction of the face. The green broken lines are the calculated energies for defects aligned along the other ⟨111⟩ directions. The legend labels the Z axis of the defect as in Table I.

and the slightly different doublet splitting observed in the spectra probably indicates a different local strain.[15]

The intensity of the 1.4-eV emission from sample B was too weak to be measured in pulsed magnetic field, where typical integration time is of the order is 2 ms. Both samples were measured using μ-PL in dc magnetic field up to 28 T. Selected representative macro- and micro-magnetophotoluminescence spectra for sample A are presented in Figs. 6(a) and 6(b), respectively. The spectra were taken in the Faraday configuration on the (111) face with $B \parallel [111]$ [Fig. 6(a)] and on the (001) face with $B \parallel [001]$ [Fig. 6(b)]. For both experimental configurations, we observe a splitting on the zero-phonon doublet into multiple lines due to the Zeeman effect. In order to compare the experimental results with the predictions of the effective spin Hamiltonian, the energy of each transition was extracted from the PL spectra by fitting a Gaussian function.

A. Macro-photoluminescence on the (111) face

Using both Faraday and Voigt configurations as appropriate, the macro-photoluminescence has been collected on the (111) face with the magnetic field aligned along the experimentally available symmetry axes of the defect [i.e., perpendicular to the face or parallel or perpendicular to certain edges of the face (see Fig. 4)]. The energy of the observed optical transitions for $B \parallel [111]$, $B \parallel [1\bar{1}0]$, and $B \parallel [11\bar{2}]$ is plotted as symbols in Figs. 7(a)–7(c). Only a few transitions are observed with most spectra showing only four lines. The simplicity of the observed spectra immediately suggests that the defect axis is preferentially aligned along the [111] growth direction of the face. NND already reported a preferential alignment of the defect axis along one of the ⟨111⟩ directions.

Making this assumption, we fit the transition energies calculated with the effective spin Hamiltonian. The configuration $B \parallel [111]$ for a defect aligned along [111], i.e., the Z axis, is a particularly easy case to fit since all the of-diagonal terms in the secular matrices are zero and only the parameters g_3 and g_3' play a role (g_3^e which controls the splitting of the excited state which is not resolved here is determined later from the high-resolution μ-PL measurements). Using

the NND parameters in Ref. 15 as a starting point, we have fitted the $B \parallel [111]$ data. Subsequently, the other orientations, $B \parallel [1\bar{1}0]$ and $B \parallel [11\bar{2}]$, were simulated to extract g_1 and g_1^e. The results of such a fit are shown by the solid red lines in Figs. 7(a)–7(c). The agreement is extremely good, apparently confirming the trigonal symmetry and preferential orientation of the defect axis along the [111] growth direction. For the [111] aligned defect, there is no difference between the $B \parallel [1\bar{1}0]$ and $B \parallel [11\bar{2}]$ orientations since these directions represent the local Y and X axes, which are equivalent. This is confirmed by the almost identical evolution of the observed transition energies for the two directions [Figs. 7(b) and 7(c)].

For $B \parallel [1\bar{1}0]$, the green broken lines are the calculated transition energies for defects with their axes aligned along the $[1\bar{1}1]$ and $[\bar{1}11]$ directions. Clearly, these transitions are not reproduced in the data. However, from this orientation we can only say that the defect is either aligned along the [111] or the $[\bar{1}\bar{1}1]$ directions for which the projection of the magnetic field onto the local axis has the same magnitude so that the transitions are degenerate (red solid lines). It is the $B \parallel [11\bar{2}]$ data which tells us definitively that the defect is aligned along [111]; the projection of the magnetic field is different for all the other ⟨111⟩ directions and the calculated transitions for the $[\bar{1}\bar{1}1]$ (purple dotted lines) defect orientation are clearly not observed.

B. Macro-photoluminescence on the (001) face

As before, using both Faraday and Voigt configurations, macro-photoluminescence has been collected on the (001) face with the magnetic field aligned along the experimentally available symmetry axes of the defect. The energy of the observed optical transitions for $B \parallel [001]$, $B \parallel [1\bar{1}0]$, and $B \parallel [110]$ is plotted as symbols in Figs. 8(a)–8(c). In contrast to the (111) face, we find that there is no preferential orientation of the defect axis. The observed transitions have been simulated using the NND effective spin Hamiltonian. This fit was performed simultaneously with the fit to the data on the (111) face, allowing a global optimization of the parameters. The parameters found are summarized in Table II.

For the $B \parallel [001]$, all the possible defect alignments are equivalent so that no information concerning a preferential orientation can be obtained form these data. Nevertheless, the predictions of the effective spin Hamiltonian (solid red lines) fit the data very nicely. More information can be gained from the $B \parallel [1\bar{1}0]$ and $B \parallel [110]$ orientations. In Figs. 8(b) and 8(c), the red solid lines correspond to defects aligned along [111] or $[\bar{1}\bar{1}1]$ and the green dashed lines to defects oriented along $[\bar{1}11]$ or $[1\bar{1}1]$ directions. In the case of a preferential alignment one of the two $B \parallel [1\bar{1}0]$ or $B \parallel [110]$ orientations would have an extremely simple spectrum composed of only four lines. This is clearly not the case; all predicted transitions are observed for both directions. Thus, at least one of the [111] or $[\bar{1}\bar{1}1]$ directions and at least one of the $[\bar{1}11]$ or $[1\bar{1}1]$ directions are occupied. The results on the (001) face suggest that the preferential alignment along the [111] direction on the (111) face may be linked to the growth process.

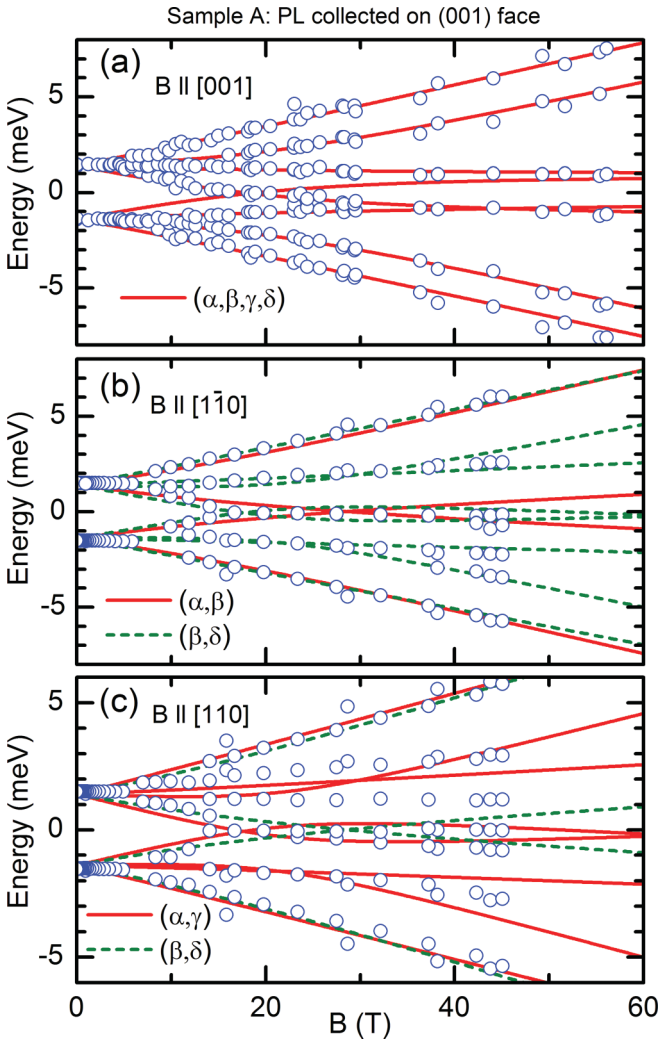

FIG. 8. (Color online) Energy of the transitions (symbols) for photoluminescence collected from the (001) face of the diamond crystal (sample A) as a function of the magnetic field applied parallel to the [001], $[1\bar{1}0]$, and [110] directions. The transition energies calculated with the effective spin Hamiltonian are shown as red solid lines for a defect axis aligned along the [111] growth direction of the face. The green broken lines are the calculated energies for defects aligned along the other ⟨111⟩ directions. The legend labels the Z axis of the defect as in Table I.

C. μ-PL measurements

The μ-PL technique is not as useful for determining the symmetry of the defect since only the Faraday configuration can be used so that the only orientation available is with the magnetic field perpendicular to the face under investigation. It does, however, have certain advantages; (i) excitation and collection is very efficient which allows the investigation of samples with a low emission intensity and (ii) spectrally resolved maps with a spatial resolution $\simeq 1$ μm can be made given information concerning the homogeneity of the diamond crystal. The μ-PL measurements have been performed at $T = 4.2$ K using a resistive magnet in static fields up to 28 T.

In Figs. 9(a) and 9(b), emission obtained from the (001) face of samples A and B is presented (symbols). The results for the two different samples are almost identical despite

TABLE II. Parameters of the effective $S = 1/2$ spin Hamiltonian found here and in previous work. The standard parameters fit the majority of the present data. The misaligned parameter set corresponds to the special case of defects on the (111) face which do not have their quantization axis preferentially aligned along the [111] growth directions. The larger estimated error for the misaligned defects is due to the restricted data set which is limited to the $B \parallel [111]$ configuration on the (111) face. Note, the NND values are twice those given in Ref. 15 due to their implicit use of an $S = 1$ Hamiltonian when writing the secular equation.

	g_3	g_3'	g_1	g_3^e	g_1^e	λ (meV)
Isoya ESR (Ref. 13)	2.329					
NND PL (Ref. 15)	2.42	1.62	1.28	0.18	2.5	2.8
Mason MCDA (Ref. 17)	2.32			<0.1	2.445	
Maes PL (Ref. 18)	(2.329)	1.93				
Standard parameters (this work)	2.3 ± 0.05	2.0 ± 0.05	1.7 ± 0.05	0.16 ± 0.03	2.4 ± 0.05	2.800
Defect misaligned on (111) face	3.5 ± 0.1	3.0 ± 0.1	1.7 ± 0.1	(0.16)	2.3 ± 0.1	2.874

the approximately two orders of magnitude larger nitrogen concentration of sample B. As the emission intensity from sample B was very weak, fewer transitions are resolved at low magnetic field. The solid red lines are the predictions of the effective spin Hamiltonian using exactly the same parameters as before. As for the macro-PL measurements, the fits are very good for a data set of much higher quality, further confirming the trigonal symmetry of the defect. For the (001) face with $B \parallel [001]$, all the defect orientations are equivalent so that no information concerning defect alignment can be extracted. The nickel concentration in the two samples is approximately equal so that the results suggest that while excess nitrogen reduces considerably the intensity of the PL emission, presumably by forming other complexes with Ni, some of the Ni nevertheless enters the host lattice as 1.4-eV Ni color centers.

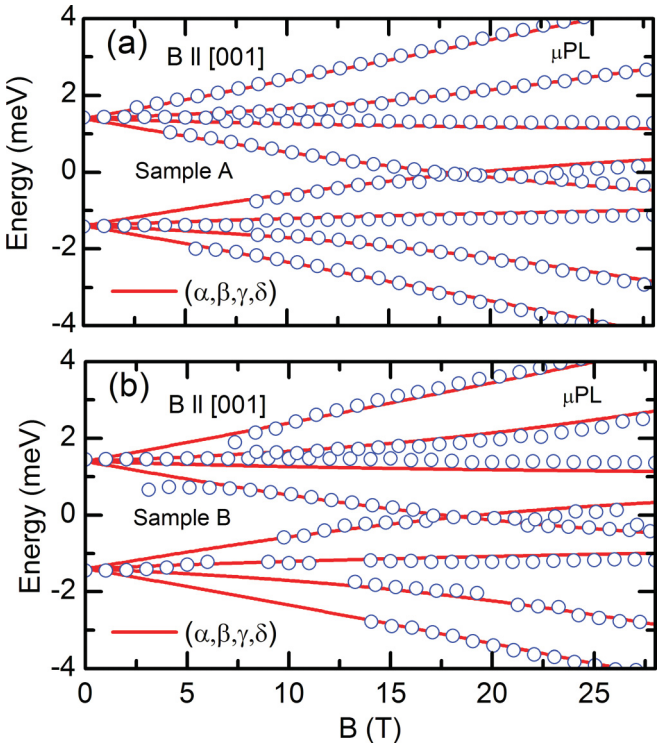

FIG. 9. (Color online) Energy of the observed transitions (symbols) for $T = 4.2$ K μ-photoluminescence collected on the (001) face with $B \parallel [001]$ on samples A and B as a function of the magnetic field. The red solid lines are the predictions of the NND effective spin Hamiltonian (all defect alignments are equivalent for $B \parallel [001]$). The legend labels the Z axis of the defect according to Table I.

Figures 10(a) and 10(b) show μ-PL measurements obtained at two different positions on the (111) face of sample A with $B \parallel [111]$. We have performed a full map of the face, and position 1 in Fig. 10(a) is representative of most of the (111) face. The behavior is identical to that observed in macro-PL. The predictions of the effective spin Hamiltonian for a defect preferentially aligned along the [111] direction are shown by the red solid lines and the other orientations by the green broken lines. The data are well fitted by the preferentially aligned defect scenario. As emission from position 1 is representative of the (111) face, this allows us to conclude that the defect is preferentially aligned along the [111] growth direction over most of the (111) face. The splitting of the excited state is also clearly seen in this high-resolution low-noise data taken in static magnetic fields. See, e.g., the splitting of the lowest- and highest-energy transition in Fig. 10(a) above 15 T. Fitting the Hamiltonian to this splitting, it is possible to extract a refined value of g_3^e, which describes the small spin splitting of the excited state with the field applied along the Z quantization axis. In Fig. 10(c), the excited-state splitting is shown; we plot the energy of the split transitions after subtracting the average energy to remove the background. A least-squares fit to both data sets (solid lines) gives $g_3^e = 0.16 \pm 0.03$. The complete set of parameters for the effective spin Hamiltonian is given in Table II. The values proposed by NND are shown for comparison. The differences are small, showing both the reproducibility of the results between different samples and the remarkable job performed by NND from limited PL data in relatively low magnetic fields $B \leqslant 6$ T.

It is, however, possible towards the bottom of the (111) face, i.e., when going far away from the $[1\bar{1}0]$ top edge (see Fig. 4), to find very different spectra as shown in Fig. 10(b). The spectra measured at position 2 contain many more lines, indicating that the defect is not preferentially aligned along the growth direction. Such spectra occur in areas of the (111) with increased intensity of emission in zero magnetic field (see Fig. 11). In addition, a radically different parameter set for the effective spin Hamiltonian is required to fit the data. We have fitted the data assuming that the defect orientation is not along the [111] growth direction (green broken lines). For $B \parallel [111]$, the three "misaligned" defect orientations are all equivalent. The extracted parameters are given in Table II. The fit is almost perfect, confirming the trigonal

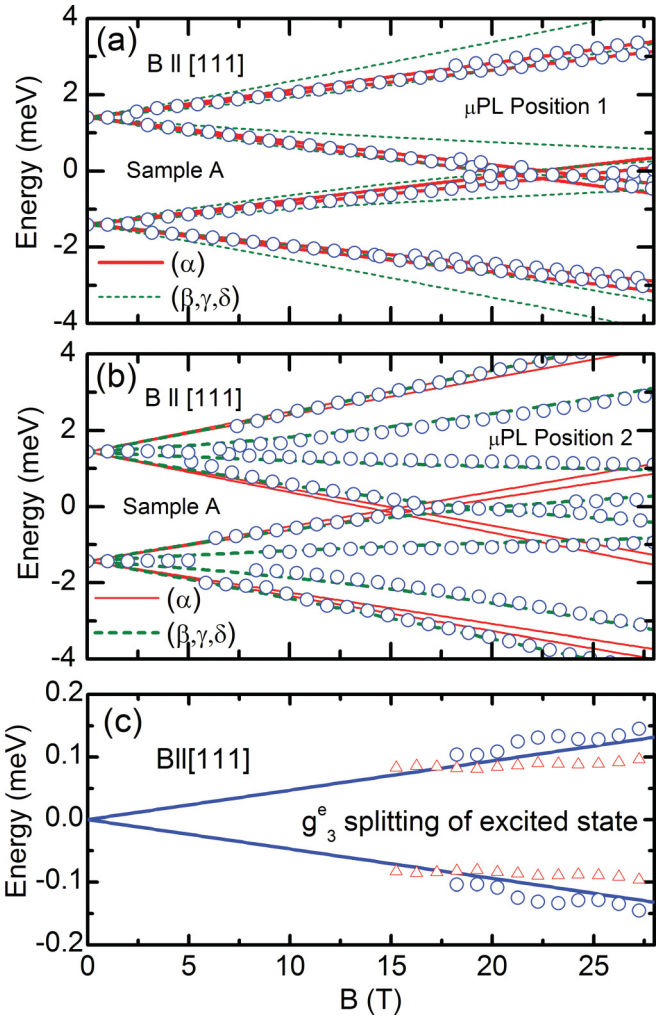

FIG. 10. (Color online) (a), (b) Energy of the observed transitions (symbols) for $T = 4.2$ K μ-photoluminescence collected at two different positions on the (111) face with $B \parallel [111]$ on sample A as a function of the magnetic field. The predictions of the NND effective spin Hamiltonian are shown for a defect preferentially aligned along [111] (red solid lines) and the other three equivalent $\langle 111 \rangle$ directions (green broken lines). Note that at position 2, the defects are not preferentially aligned along the growth direction and fitting requires a radically different set of parameters. (c) Splitting of the excited state; the high- (circles) and low- (triangles) energy transitions in (a), from which the average energy of the transition has been subtracted, are plotted versus magnetic field. The solid lines are a least-squares fit to extract $g_3^e = 0.16 \pm 0.03$.

symmetry. The red solid lines are the prediction for a defect aligned along the [111] growth direction. From the data above 20 T, it appears that these transitions are completely absent from the spectra. This suggests that the defect may even be preferentially "not aligned" with the growth direction in this region of the face, which is close to the seed crystal. Moreover, the parameters required to fit are considerably different from those obtained previously. In particular, the values of g_3 and g_3' are ~50% larger, reflecting the much larger Zeeman splitting of the ground state even though the magnetic field is not aligned along the Z quantization axis. This suggests that the local environment (trigonal distortion) of the

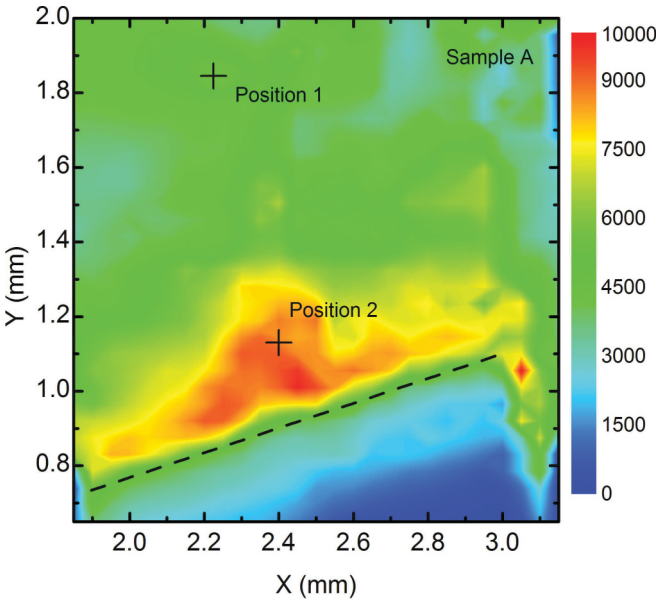

FIG. 11. (Color online) Spatial PL map of the (111) face measured at $T = 4.2$ K and $B = 0$ T showing the integrated intensity of the high-energy component of the 1.4-eV doublet. The dashed line indicates the bottom of the (111) face. Intensity decreases rapidly below this line due to the loss of focus. The positions at which the μ-PL spectra in Fig. 5 were taken are indicated.

Ni center is significantly different in regions of the (111) face where it does not preferentially align along the [111] growth direction.

V. DISCUSSION

The 1.4-eV Ni center investigated here has been unambiguously identified with the NIRIM-2 ESR line in HPHT diamond.[14,15] NIRIM-2 has a large angular dependence of the magnetic field position of the ESR lines, which is consistent with the center having trigonal symmetry.[13] ESR gives very precise values for the anisotropic g factor, but due to occupation effects at the low temperatures used, probes only the (Zeeman) splitting of the lower energy level of the ground-state doublet, i.e., $E_2 - E_1$ in Eq. (7). While magnetic circular dichroism (MCDA) is a less precise technique, it is extremely useful since it gives access to the g factors of the excited state.[17] The measured anisotropy of the g factor can provide a crucial test for a given microscopic model. In Fig. 12, we show the ground-state splitting (effective g factor) obtained from the ESR data of Isoya *et al.*[13] together with the MCDA results of Mason *et al.*[17] for the excited-state splitting. The expected angular dependence of the ground-state splitting using the effective spin Hamiltonian is also plotted for the ground (solid lines) and excited state (broken line) as a function of angle when the magnetic field is rotated around the $[\bar{1}10]$ direction, e.g., from $B \parallel [001]$ to $B \parallel [11\bar{2}]$. The predictions of the effective spin Hamiltonian are in excellent agreement with the ESR and MCDA results for both the ground and excited states.

In order to compare the g factors of the effective spin Hamiltonian with the ESR and MCDA results, it is convenient to define effective (ESR) g factors $g_\parallel$ and $g_\perp$ corresponding

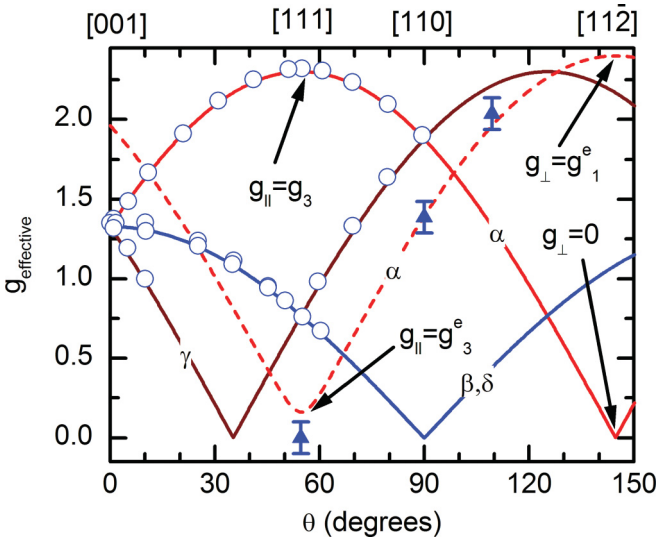

FIG. 12. (Color online) The circles show the angular dependence of the line position (effective g factor) of the NIRIM-2 center, taken from Ref. 13, with the magnetic field rotated about the [$\bar{1}$10] axis at $T = 4$ K and $B \simeq 0.5$ T. The triangles are the splitting of the excited state measured using MCDA taken from Ref. 17. Also shown is the predicted angular dependence of the ground-state splitting (solid lines) and excited-state splitting (broken lines), calculated using the effective spin Hamiltonian with the parameters found in this work, and given in Table II. The curves are labeled according to the alignment of the defect Z quantization axis.

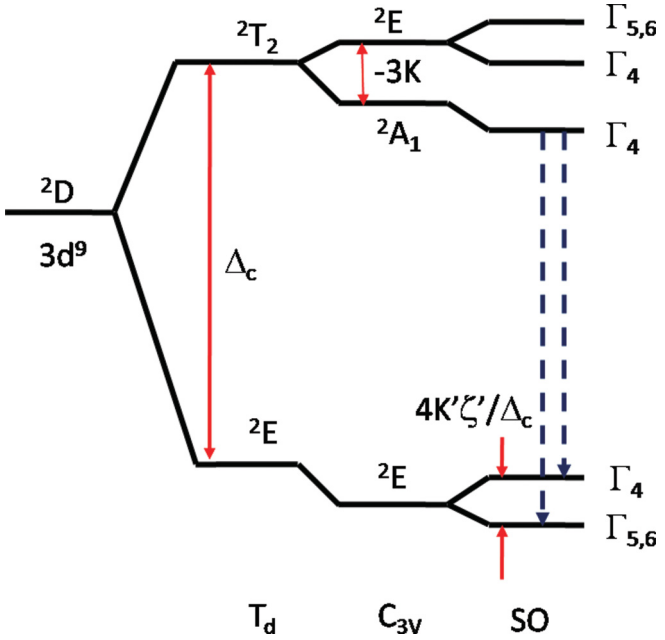

FIG. 13. (Color online) Energy levels of the ^2D state of $3d^9$ interstitial Ni^+ showing the subsequent effects of the cubic (T_d) and trigonal (C_{3v}) crystals fields and spin-orbit interaction (Ref. 17). The broken arrows indicate the observed zero-field optical transitions.

to a magnetic field aligned parallel and perpendicular to the Z quantization axis of the defect. For the ground-state splitting $E_2 - E_1$, we have a large $g_{\|} = g_3$ and $g_{\perp} = 0$. Note that the magnetic field component which is not along Z does not generate a Zeeman splitting of the ground state. The B_X and B_Y components only change the splitting of the zero-field doublet, as can be seen from Eq. (7). The situation for the excited state is very different with a small $g_{\|} = g^e_3$ and a large $g_{\perp} = g^e_1$. As pointed out by Mason *et al.*, the very small value of $g_{\|} \approx 0$ is a most unexpected result for an orbital singlet state.[17] The high magnetic field PL results presented here have allowed a rather precise determination of the g factors, which motivates us to revisit Mason *et al.*'s quantitative comparison with the g factors derived from the crystal-field theory of interstitial $3d^9$ Ni^+.

A. Crystal-field model

It has been proposed that the Hamiltonian used for neutral substitutional vanadium in SiC (Ref. 26) can also be applied to the case of interstitial Ni^+,[17]

$$H = H_{T_d} + H_{C_{3v}} + H_{SO} + H_Z, \tag{8}$$

where H_{T_d} contains the cubic crystal field term, $H_{C_{3v}}$ the trigonal crystal field, H_{SO} the spin-orbit interaction, and finally H_Z includes the Zeeman interaction. The resulting level structure is shown in Fig. 13. The parameters Δ_c, K, ζ, and k are the cubic crystal-field splitting, one-third of the trigonal crystal-field splitting within the $^2T_2$ state, the spin-orbit parameter, and an orbital reduction factor, respectively (K', ζ', and k' are the corresponding quantities for the ^2E state).

The sign of the $^2T_2$ trigonal crystal-field parameter $K < 0$ is chosen so that the A_1 level of the excited state is lowest in agreement with the uniaxial stress measurements[15] and the spin-orbit parameters ζ and ζ' are both negative for the single d^9 hole.

The ^2E ground state is split into two Kramers doublets by a combination of spin-orbit coupling and trigonal distortion:

$$\lambda = E(\Gamma_4) - E(\Gamma_{5,6}) = \frac{4\zeta' K'}{\Delta_c}, \tag{9}$$

where the cubic crystal-field term $\Delta_c \simeq 1.4$ eV. From the measured splitting $\lambda = 2.8$ meV, we obtain the product $\zeta' K' = 0.98 \times 10^{-3}$ eV^2.

The g factors of the ground-state doublet are for the $\Gamma_{5,6}$ state[17]

$$\begin{aligned} g_{\|} &= g_3 = 2 - \frac{4k'\zeta'}{\Delta_c} - \frac{8k'K'}{\Delta_c}, \\ g_{\perp} &= 0, \end{aligned} \tag{10}$$

and for the Γ_4 state

$$\begin{aligned} g_{\|} &= g'_3 = 2 - \frac{4k'\zeta'}{\Delta_c} + \frac{8k'K'}{\Delta_c}, \\ g_{\perp} &= \frac{4k'\zeta'}{\Delta_c}. \end{aligned} \tag{11}$$

As $\Delta_c \gg K', \zeta'$ the Γ_4 state has $g_{\perp} \approx 0$ so that the effective spin Hamiltonian (in which *de facto* $g_{\perp} = 0$) is a reasonable approximation. Using the values of $g_3 = 2.3$ and $g'_3 = 2.0$ found in this work, solving Eqs. (10) and (11) immediately gives $4k'\zeta'/\Delta_c = 8k'K'/\Delta_c = -0.15$ so that $g_{\perp} = -0.15$. Although small, the splitting of the upper doublet state should be experimentally observable at magnetic fields above 15 T

with B applied perpendicular to the Z defect axis on the [111] face. The high-resolution μ-PL measurements, with narrower line widths and better signal/noise in static magnetic fields, clearly resolved the similarly small splitting of the excited state with $B \parallel Z$. Unfortunately, only the Faraday configuration is possible when using the μ-PL system so that such a measurement is excluded for the present. Making the approximation that the orbital reduction factor $k' \approx 1$ gives $K' = \zeta'/2 = 0.0262$ eV. As pointed out by Mason *et al.*, while such values of ζ' and K' are reasonable, the product $\zeta' K' = 1.4 \times 10^{-3}$ eV^2 is too large to be compatible with the $\zeta' K' \simeq 1 \times 10^{-3}$ eV^2 obtained from Eq. (9) knowing the spin-orbit splitting $\lambda = 2.8$ meV of the zero-field doublet. Using an orbital reduction factor $k' < 1$ only makes the situation worse.

The g factors of the excited state (lower Γ_4 of $^2T_2$) are given by[17]

$$\begin{aligned} g_\parallel &= g_3^e = 2(a^2 - b^2) - 2kb^2, \\ g_\perp &= g_1^e = 2a^2 - 2\sqrt{2}kab, \end{aligned} \tag{12}$$

where

$$\begin{aligned} a &= \cos(\gamma), \quad b = -\sin(\gamma), \\ \gamma &= \frac{\zeta/\sqrt{2}}{3K/2 - \zeta/4}. \end{aligned} \tag{13}$$

The cos and sin terms give an additional constraint that $a^2 + b^2 = 1$, so that the orbital reduction factor k can not be freely chosen. Using the values of $g_3^e = 0.16$ and $g_1^e = 2.4$ found in this work, a solution to Eq. (12) exists with $k = 0.79$, $a = 0.82$, and $b = -0.574$. From Eq. (13), this implies that $K \simeq \zeta/3.5$. Neglecting covalency effects, which are expected to be small in diamond, $\lambda \approx \lambda'$ giving $K \approx 0.015$ eV.

Thus, the only apparent shortcoming of the crystal-field model is its inability to correctly predict the zero magnetic field doublet splitting. It has been suggested that this might be explained by corrections to the splitting of the ^2E state which can arise due to a mixing with the $4p$ states of the Ni$^+$.[27] Such a mechanism has also been proposed for $3d^9$ Cu^{2+} in II-VI compounds.[28,29]

A crucial test of the crystal-field model is provided by defects with a quantization axis which is not preferentially aligned: In the μ-PL data, it is possible to find regions of the (111) face towards the bottom of the sample, i.e., near the seed crystal, where the defects are not preferentially aligned along the [111] growth direction. Such defects have an almost identical emission energy (see Fig. 5) and an almost identical splitting ($\lambda = 2.874$ meV) of the zero magnetic field doublet. Surprisingly, the g factors for the trigonal axis of such defects are markedly different (see Table. II). Using the values found in experiment, $g_3 = 3.5$ and $g_3' = 3.0$ in Eqs. (10) and (11), gives $4k'\zeta'/\Delta_c = -1.25$ and $8k'K'/\Delta_c = -0.25$ so that $K' = \zeta'/10$. Assuming $k' \approx 0$, the spin-orbit coupling term $\zeta' \simeq 0.44$ eV and trigonal crystal-field term $K' \simeq 0.044$ eV. The value of ζ' is an unreasonable six times larger that the value of 0.075 eV for a free Ni$^+$ ion.[17,30] Moreover, the product $\zeta' K' \simeq 20 \times 10^{-3}$ eV^2 overestimates the zero-field doublet splitting [Eq. (9)] by over an order of magnitude. At the same time, experiment indicates that the splitting of the zero-field doublet is almost unchanged. This forces us to conclude that the crystal-field model does not provide a correct quantitative description of the 1.4-eV Ni color center in diamond.

VI. CONCLUSION

We have investigated two different boron-free HTHP synthetic diamond crystals. Our high magnetic field photoluminescence results are perfectly described by the NND effective spin Hamiltonian, unequivocally demonstrating the trigonal symmetry of the 1.4-eV Ni color center in diamond. Both samples investigated have a similar Ni content ($\simeq 1 \times 10^{19}$ cm^{-3}) but radically different concentrations of N. Sample B has a similar concentrations of Ni and N, while sample A has roughly two orders of magnitude less nitrogen. Magnetization measurements show that Ni is predominantly incorporated into sample B as isolated Ni complexes and into sample A as nm-size Ni clusters. Nevertheless, both samples exhibit the characteristic 1.4-eV emission doublet associated with an isolated Ni complex. Thus, there seems to be no correspondence between the macroscopic (magnetic) properties of a given sample and the incorporation of Ni color centers. Despite the significantly lower concentration of isolated Ni, sample A shows much stronger 1.4-eV emission. This suggests that the presence of N does not necessarily favor the formation of the 1.4-eV Ni color center; the concentration of isolated Ni-N complexes is almost certainly higher in sample B, while the 1.4-eV PL signal is much weaker, suggesting that the presence of N may actually impede the formation of this particular Ni color center. As nitrogen is usually a donor in diamond, a possible mechanism could be the transfer of a donor electron to the Ni$^+$ ion reducing the number of optically active centers.[27,31]

The magneto-PL presented here, together with previously published magneto-PL and PL under uniaxial stress,[15,18] ESR,[13] and MCDA (Ref. 17) are all consistent with an interstitial $3d^9$ Ni$^+$ with spin $S = 1/2$ and a large trigonal distortion (C_{3v} symmetry) due to a displacement of the Ni along a $\langle 111 \rangle$ direction. The exact nature of the complex nevertheless remains unknown. A complex involving an additional, transition-metal impurity, dopants such as nitrogen or boron, or a vacancy or divacancy, are required to produce the trigonal distortion. On the basis of the ESR results, Isoya *et al.* suggested an interstitial Ni$^+$-vacancy complex. However, this configuration has been shown to be unstable[20] with the interstitial Ni moving towards vacancy, i.e., to the substitutional site. First-principles calculations suggest that a complex involving boron and substitutional nickel fulfills all the necessary requirements.[21] However, this assignment seems to be unlikely here as there was no boron present in the melt during the growth of our samples. Moreover, recent density functional theory (DFT) calculations coupled with x-ray absorption spectroscopy measurements performed on sample B suggest the incorporation of nickel as a divacancy complex, in which interstitial Ni is placed at the midpoint between two vacancies.[32] However, the first-principles calculations of Larico *et al.*[21] suggest that the (VNiV)$^+$ complex has C_{2h} symmetry with the Ni-related electronic states resonant and inert inside the valence band. First-principles calculations of

defects in diamond are in general complicated due to the need to take into account possible relaxations of neighboring carbon atoms, which can alter both the energy and the symmetry of the center. Under such conditions, the microscopic model for the 1.4-eV Ni color center in diamond should still be considered as an open question.

ACKNOWLEDGMENTS

The help of F. Donatini with the cathodoluminescence measurements is gratefully acknowledged. We thank L. Eaves and B. Clerjaud for their interest in this work and stimulating discussions. This work was partially supported by EuroMagNET II under the EU Contract No. 228043.

*paulina.plochocka@lncmi.cnrs.fr

[1] I. Aharonovich, S. Castelletto, D. A. Simpson, A. Stacey, J. McCallum, A. D. Greentree, and S. Prawer, Nano Lett. **9**, 3191 (2009).

[2] I. Aharonovich, C. Zhou, A. Stacey, J. Orwa, S. Castelletto, D. Simpson, A. D. Greentree, F. Treussart, J.-F. Roch, and S. Prawer, Phys. Rev. B **79**, 235316 (2009).

[3] D. A. Simpson, E. Ampem-Lassen, B. C. Gibson, S. Trpkovski, F. M. Hossain, S. T. Huntington, A. D. Greentree, L. C. L. Hollenberg, and S. Prawer, Appl. Phys. Lett. **94**, 203107 (2009).

[4] S. Castelletto, I. Aharonovich, B. C. Gibson, B. C. Johnson, and S. Prawer, Phys. Rev. Lett. **105**, 217403 (2010).

[5] J. J. L. Morton, Nat. Phys. **2**, 365 (2006).

[6] J. R. Maze, P. L. Stanwix, J. S. Hodges, S. Hong, J. M. Taylor, P. Cappellaro, L. Jiang, M. V. G. Dutt, E. Togan, A. S. Zibrov, A. Yacoby, R. L. Walsworth, and M. D. Lukin, Nature (London) **455**, 644 (2008).

[7] G. Balasubramanian, I. Y. Chan, R. Kolesov, M. Al-Hmoud, J. Tisler, C. Shin, C. Kim, A. Wojcik, P. R. Hemmer, A. Krueger, T. Hanke, A. Leitenstorfer, R. Bratschitsch, F. Jelezko, and J. Wrachtrup, Nature (London) **455**, 648 (2008).

[8] A. Lohrmann, S. Pezzagna, I. Dobrinets, P. Spinicelli, V. Jacques, J.-F. Roch, J. Meijer, and A. M. Zaitsev, Appl. Phys. Lett. **99**, 251106 (2011).

[9] S. C. Lawson, H. Kanda, K. Watanabe, I. Kiflawi, Y. Sato, and A. T. Collins, J. Appl. Phys. **79**, 4348 (1996).

[10] A. T. Collins and P. M. Spear, J. Phys. D: Appl. Phys. **15**, L183 (1982).

[11] A. M. Zaitsev, Phys. Rev. B **61**, 12909 (2000).

[12] T. Dietl, H. Ohno, and F. Matsukura, Phys. Rev. B **63**, 195205 (2001).

[13] J. Isoya, H. Kanda, and Y. Uchida, Phys. Rev. B **42**, 9843 (1990).

[14] G. Davies, A. J. Neves, and M. H. Nazaré, Europhys. Lett. **9**, 47 (1989).

[15] M. H. Nazaré, A. J. Neves, and G. Davies, Phys. Rev. B **43**, 14196 (1991).

[16] K. Iakoubovskii and G. Davies, Phys. Rev. B **70**, 245206 (2004).

[17] P. W. Mason, F. S. Ham, and G. D. Watkins, Phys. Rev. B **60**, 5417 (1999).

[18] J. Maes, K. Iakoubovskii, M. Hayne, A. Stesmans, and V. V. Moshchalkov, J. Phys. D: Appl. Phys. **37**, 1102 (2004).

[19] J. M. Baker, J. Phys.: Condens. Matter **15**, S2929 (2003).

[20] R. Larico, L. V. C. Assali, W. V. M. Machado, and J. F. Justo, Appl. Phys. Lett. **84**, 720 (2004).

[21] R. Larico, J. F. Justo, W. V. M. Machado, and L. V. C. Assali, Phys. Rev. B **79**, 115202 (2009).

[22] J. Isoya, H. Kanda, J. R. Norris, J. Tang, and M. K. Bowman, Phys. Rev. B **41**, 3905 (1990).

[23] M. Nazaré, J. Lopes, and A. Neves, Phys. B (Amsterdam) **308–310**, 616 (2001).

[24] L. Eaves and C. Uihlein, J. Phys. C: Solid State Phys. **15**, 6257 (1982).

[25] C. Uihlein and L. Eaves, Phys. Rev. B **26**, 4473 (1982).

[26] B. Kaufmann, A. Dörnen, and F. S. Ham, Phys. Rev. B **55**, 13009 (1997).

[27] L. Paslovsky and J. E. Lowther, J. Phys.: Condens. Matter **4**, 775 (1992).

[28] U. Scherz, J. Phys. Chem. Solids **30**, 2077 (1969).

[29] T. Telahun, U. Scherz, P. Thurian, R. Heitz, A. Hoffmann, and I. Broser, Phys. Rev. B **53**, 1274 (1996).

[30] C. Moore, *Atomic Energy Levels*, Natl. Bur. Stand. (US) Circ. No. 467 (US GPO, Washington DC, 1949).

[31] A. T. Collins, H. Kanda, and R. C. Burns, Philos. Mag. Part B **61**, 797 (1990).

[32] E. Gheeraert, A. Kumar, J. Pernot, L. Magaud, Y. Joly, E. Bustarret, S. Pascarelli, M. Ruffoni, H. Kanda, and D. Avasthi (unpublished).